

Article

# Finite Element Analysis of Thermo-Diffusion and Multi-Slip Effects on MHD Unsteady Flow of Casson Nano-Fluid over a Shrinking/Stretching Sheet with Radiation and Heat Source

Liaqat Ali <sup>1</sup> , Xiaomin Liu <sup>1,\*</sup>, Bagh Ali <sup>2</sup> , Saima Mujeed <sup>3</sup> and Sohaib Abdal <sup>4</sup>

<sup>1</sup> School of Energy and Power, Xi'an Jiaotong University, No.28 West Xianning Road, Xi'an 710049, China; math1234@stu.xjtu.edu.cn

<sup>2</sup> Department of Applied Mathematics, Northwestern Polytechnical University, Dongxiang Road, Beilin District, Xi'an 710129, China; baghalisewag@mail.nwpu.edu.cn

<sup>3</sup> School of Management, Xi'an Jiaotong University, No.28 West Xianning Road, Xi'an 710049, China; hamzaxjtu@gmail.com

<sup>4</sup> School of Mathematics, Northwest University, No.229 North Taibai Avenue, Xi'an 710069, China; sohaibabdal8@gmail.com

\* Correspondence: liuxm@xjtu.edu.cn;

Received: 22 September 2019; Accepted: 26 November 2019; Published: 30 November 2019



**Abstract:** In this article, we probe the multiple-slip effects on magnetohydrodynamic unsteady Casson nano-fluid flow over a penetrable stretching sheet, sheet entrenched in a porous medium with thermo-diffusion effect, and injection/suction in the presence of heat source. The flow is engendered due to the unsteady time-dependent stretching sheet retained inside the porous medium. The leading non-linear partial differential equations are transmuted in the system of coupled nonlinear ordinary differential equations by using appropriate transformations, then the transformed equations are solved by using the variational finite element method numerically. The velocity, temperature, solutal concentration, and nano-particles concentration, as well as the rate of heat transfer, the skin friction coefficient, and Sherwood number for solutal concentration, are presented for several physical parameters. Next, the effects of these various physical parameters are conferred with graphs and tables. The exact values of flow velocity, skin friction, and Nusselt number are compared with a numerical solution acquired with the finite element method (FEM), and also with numerical results accessible in literature. In the end, we rationalize the convergence of the finite element numerical solution, and the calculations are carried out by reducing the mesh size.

**Keywords:** MHD; FEM; Casson nano-fluid; heat source; multiple slip; porous medium

## 1. Introduction

The basic idea of the non-slip condition is concerned with the Navier Stokes theory. To study the temperature and velocity, numerous authors have found both the analytical and numerical solution by the implementation of non-slip boundary conditions. The utmost significance of slip-conditions in nano-channels has stimulated, to a great extent, interest in the study of vibrating values [1]. Now it is not unknown that if fluid contains concentrated suspensions, in that case the slip could be stirring. Soltani and Yilmazer [2] have performed by parallel disk rheometer with prominence on the wall slip phenomena on the rheological characterization of extremely filled suspensions consisting of Newtonian matrix and diverse with two different power sizes of aluminum and two different sizes of bed glass. In the articulations of fluid-like as suspension, emulsion foams, and polymer solution,

partial velocity slip can occur on the stretching boundary. In an assortment of industry procedures, the influences of slip can crop-up at the boundary of pipes, surfaces, and walls. The Navier Stoke velocity slip conditions are customary to approach in the study of slip phenomenon.

There are hundreds of applications in industries and engineering, and magneto-hydrodynamic fluid flows through stretching sheet have achieved much importance in recent days, according to Mabbod et al. [3]. Applications as well as the liquid coating on the photographic films, boundary layers throughout the liquid film in the concentration procedure, and the aerodynamic excrescence of plastic sheets exist. With this, the extensive range of applications of magnetohydrodynamic flow that can be found in copious fields like in electronic cooling process, in boilers, heat lagging, and metal extrusion, geothermal system, nuclear process, micro-magnetohydrodynamic pumps, underground water system, in energy storage units, biological conveyance, and in the thermal energy procedure has played a very important role. Unsteady flow due to the stretching sheet has been scrutinized by Pop and Na [4]. Afterward, Sheridan et al. [5] investigated the significance of variable wall temperature and variable heat flux in the boundary layer flow over the unsteady stretching surface with similarity transformation. An unsteady stagnation point flow of the viscous fluid caused by a stretching sheet under the influence of slip condition has been reported by Bhattacharyya et al. [6]. The impact of the magnetic field on the two-dimensional flow of nano-fluid with and without slip condition was conferred by Khan et al. [7] and Mohyud-Din et al. [8,9], correspondingly. Khan et al. [10] investigated two-dimensional electrically conducting a flow of nano-fluid due to the stretching sheet under the impact of convective boundary condition.

The wide-ranging applications of non-Newtonian liquids in numerous industries such as molten plastics, nuclear waste disposal, artificial fibers, foodstuffs, transpiration cooling, and petroleum reservoirs have gained fascination to analyze their characteristic comportment. Casson fluid is one sort of fluid model for non-Newtonian fluid. Casson fluid has an inestimable viscosity at zero rates of shear and have zero viscosity at an infinite rate of shear and the yield stress under which there is no flow occurs. Consequently, Casson-fluid could be defined such as shear-thinning liquid or pseudo-plastic fluid. The flow characteristic of blood can precisely be defined by Casson fluid at the small shear rates. Sharada and Shankar [11] scrutinized numerically Soret and Dufour effects, thermal radiation, and chemical reaction on fluid flow, and heat and mass transfers of Casson fluid over an exponentially stretching surface. Ullah et al. [12] observed that unsteady MHD diverse convection slip flow of Casson fluid towards non-linearly stretching sheet soaked in a porous medium in existence of slip and convective boundary conditions occurs. Furthermore, Ullah et al. [13] acquired numerical results for hydro-magnetic Falkner Skan flow of the Casson fluid past a moving wedge, along with heat transfer. Pushpalatha et al. [14] deliberated thermal diffusion effects and radiation on Casson-fluid flow with convective boundary conditions. Pushpalatha et al. [15] deliberated the thermos-diffusion consequences on the Casson fluid over an unsteady stretching surface in the existence of thermal radiations and the magnetic field. They found that the Casson parameters and unsteadiness parameter have the propensity to denigrate the velocity dissemination. Uddin et al. [16] studied the free convective boundary layer flow of nano-fluid over a penetrable upward horizontal plate in a porous medium with thermal convective boundary conditions.

Recently, Rahman et al. [17] explored the hydro-magnetic slip flow of water-based nano-fluid over a wedge with a convective surface in the existence of heat generation or absorption. Ibrahim and Shankar [18] analyzed magneto-hydrodynamic boundary layer flow and heat transfer of nano-fluid past over penetrable stretching sheet using velocity, thermal, and solute slip boundary conditions. Das [19] presented an imperative numerical inquiry on the convective heat transfer performance of nanofluids over a penetrable stretching surface in the presence of partial slip, thermal buoyancy, and internal heat generation/absorption. The transfer of heat, investigated through the thermal radiation, has enormous applications in different technical processes, satellites, nuclear power-plants, astronomical vehicles, gas turbines, comprising missiles, and in several propulsion devices for jets. Linear radiations are not systematically in effect for the enormous temperature alteration.

Abbas et al. [20] deliberated the consequences of radiation in the existence of a uniform magnetic field of nano-fluid on the curved stretching surface by integrating the slip effect. In recent times, Makinde et al. [21] deliberated a numerical study of the effects of radiation on chemically reacting MHD nano-fluid prejudiced by the heat source/sink, and the collective heat and mass transfer analysis aimed at mixed convection flow over the vertical surface, with radiation and chemical reaction explained by Ibrahim et al. [22]. Prasannakumara et al. [23] deliberated the velocity slip effects, temperature jump, solutal slip, and thermal radiation, on steady flow, and the transfer of heat and mass of incompressible Jeffrey nano-fluid over the horizontal stretching surface. Imtiaz et al. [24] scrutinized the unsteady MHD flow of the curved stretching surface.

The literature remains silent whether we have to investigate the impact of multiple slips on MHD unsteady Casson nano-fluid flow, heat, and mass transfer in the presence of heat source with thermo-diffusion effect over a stretching/shrinking sheet. The objective of this article was to prolong the recent work of Fazle Mabood and Standford Shateyi [25]. Appropriate similarities have been used for transformation, and the governing non-linear partial differential equations are rendered in the non-dimensional and non-linear system of ODEs. The resulting system of non-linear ODEs has been solved numerically with an efficient and validated variational finite element method (FEM) with the boundary conditions. We also use a special case for the existing model to compare our outcomes along with previous studies. A parametric study has been performed to inquire into the mass and heat transfer characteristics and also the impact of different parameters of the flow. After that, we have provided a numerical comparison of our results and discussed them with graphs. In future studies, transient flow with slip effects in the presence of mixed convection and chemical reaction at the sheet can be examined.

## 2. Mathematical Modeling

The unsteady two-dimensional MHD flow of an incompressible fluid and Casson nano-fluid viscous flow over an electrically conducted stretching/shrinking sheet in the presence of heat source was considered. We choose an  $xy$ -ordinate system as the measurement of the sheet will be taken with  $x$ -,  $y$ -axis, and the  $y$ -axis along the vertical direction of the sheet, as given in Figure 1. The sheet is moving with non-uniform velocity  $U(x, t) = ax / (1 - \lambda t)$  since  $a$  is the stretching rate along the  $x$ -axis but  $\lambda t$  is positively constant, as by property  $\lambda t < 1$ . The transverse magnetic field is supposed be the function of distance from the origin and is defined as  $B(x) = B_0\sqrt{x}$  with  $B_0 \neq 0$ , where  $B_0$  is the strength of the magnetic field. The induced magnetic field is negligible as compared to the applied magnetic field. The free stream temperature is supposed to be  $T_\infty$ , the free mass concentration is  $C_\infty$ , and the nano-particle concentration is  $E_\infty$ . The governing equations for flow can be put into the form as in ([25,26])

$$\frac{\partial u}{\partial x} + \frac{\partial v}{\partial y} = 0, \tag{1}$$

$$\begin{aligned} &\frac{\partial u}{\partial t} + u \frac{\partial u}{\partial x} + v \frac{\partial u}{\partial y} \\ &= \nu \left(1 + \frac{1}{\beta}\right) \frac{\partial^2 u}{\partial y^2} - \frac{\sigma B^2(x)u}{\rho} + g\beta_T(T - T_\infty) + g\beta_C(C - C_\infty) + g\beta_E(E - E_\infty) - \frac{\nu}{\kappa} u \end{aligned} \tag{2}$$

$$\begin{aligned} &\frac{\partial T}{\partial t} + u \frac{\partial T}{\partial x} + v \frac{\partial T}{\partial y} \\ &= \alpha \left(1 + \frac{16T_\infty^3 \sigma^*}{3k^* \kappa}\right) \frac{\partial^2 T}{\partial y^2} + \tau [D_B \frac{\partial E}{\partial y} \frac{\partial T}{\partial y} + \frac{D_T}{T_\infty} (\frac{\partial T}{\partial y})^2] + \frac{Q(T - T_\infty)}{\rho c_p} + D_{TC} \frac{\partial^2 C}{\partial y^2} \end{aligned} \tag{3}$$

$$\frac{\partial C}{\partial t} + u \frac{\partial C}{\partial x} + v \frac{\partial C}{\partial y} = D_m \frac{\partial^2 C}{\partial y^2} + D_T \frac{\partial^2 T}{\partial y^2} \tag{4}$$

$$\frac{\partial E}{\partial t} + u \frac{\partial E}{\partial x} + v \frac{\partial E}{\partial y} = D_B \frac{\partial^2 E}{\partial y^2} + \frac{D_T}{T_\infty} \frac{\partial^2 T}{\partial y^2} \tag{5}$$

where  $x$  and  $y$  are the co-ordinates in the  $x$ -axis and  $y$ -axis;  $u$  and  $v$  are the velocity components along the  $x$ -axis and  $y$ -axis respectively;  $\alpha$ ,  $\nu$ ,  $\sigma$ ,  $\rho$  are the thermal diffusivity, kinetic viscosity,

electrical conductivity, and density of fluid, respectively;  $g$  is the acceleration due to gravity;  $\beta_T$  is the thermal expansion coefficient;  $\beta_C$  is the solutal concentration expansion coefficient;  $\beta_E$  is the nano-particle concentration expansion coefficient;  $T$  is the temperature;  $C$  is the solutal concentration;  $E$  is the nano-particle concentration;  $D_M$  is the molecular diffusivity;  $D_T$  is the thermal diffusivity;  $D_B$  is the Brownian diffusivity;  $\sigma^*$  is the Stefan-Boltzmann constant;  $k^*$  is the mean absorption coefficient;  $T_\infty$  is the stream temperature;  $Q$  is the uniform volumetric heat generation/absorption;  $C_p$  is the specific heat of fluid;  $C_s$  is the concentration of susceptibility; and  $K_T$  is the thermal diffusion ratio. The boundary conditions for the above mathematical model are (see [25]):

$$u = U(x, t) + U_{slip}, v = v_w, T = T_w(x, t) + T_{slip}, C = C_w(x, t) + C_{slip}, E = E_w(x, t) + E_{slip},$$

$$as \quad y = 0 \tag{6}$$

$$u \rightarrow 0, T \rightarrow T_\infty, C \rightarrow C_\infty, E \rightarrow E_\infty, \quad as \quad y \rightarrow \infty, \tag{7}$$

where  $x$  and  $y$  are the co-ordinates;  $u$  and  $v$  are the velocity components along the  $x$ -axis and  $y$ -axis, respectively;  $\alpha, \nu, \sigma, \rho$  are the thermal diffusivity, kinetic viscosity, electrical conductivity and density of fluid, respectively;  $g$  is the acceleration due to gravity;  $\beta_T$  is thermal expansion coefficient;  $\beta_C$  is the solutal concentration expansion coefficient;  $\beta_E$  is the nano-particle concentration expansion coefficient;  $T$  is the temperature;  $C$  is the solutal concentration;  $E$  is the nano-particle concentration;  $D_M$  is the molecular diffusivity;  $D_T$  is the thermal diffusivity;  $D_B$  is the Brownian diffusivity;  $\sigma^*$  is the Stefan-Boltzmann constant;  $k^*$  is the mean absorption coefficient;  $T_\infty$  is the stream temperature;  $Q$  is the uniform volumetric heat generation/absorption;  $C_p$  is the specific heat of fluid;  $C_s$  is the concentration of susceptibility; and  $K_T$  is the thermal diffusion ratio.

Where the injection/suction velocity as  $v_w = v_0/\sqrt{x}$ ,  $T_w(x, t)$  is the temperature of sheet and  $C_w(x, t), E_w(x, t)$  are concentrations at surface of the below form (see [25]):

$$T_w(x, t) = T_\infty + T_0 \left( \frac{ax}{2\nu(1-\lambda t)^2} \right)$$

$$C_w(x, t) = C_\infty + C_0 \left( \frac{ax}{2\nu(1-\lambda t)^2} \right)$$

$$E_w(x, t) = E_\infty + E_0 \left( \frac{ax}{2\nu(1-\lambda t)^2} \right)$$

where  $T_0, C_0,$  and  $E_0$  are the reference temperature, reference solutal concentration, and reference nano-particle concentration respectively, such that  $0 \leq T_0 \leq T_w, 0 \leq C_0 \leq C_w$  and  $0 \leq E_0 \leq E_w,$  with these above expressions being valid if  $(1 - \lambda t) > 0$ .

Usually, the stream function  $\Psi$  is defined as  $u = \frac{\partial \Psi}{\partial y}$  and  $v = -\frac{\partial \Psi}{\partial x}$  that the Equation (1) is satisfied. We introduce similarity transformations to solve the above equations (see [25,26]):

$$\eta = \sqrt{\frac{a}{\nu(1-\lambda t)}}y, \quad \psi = \sqrt{\frac{av}{(1-\lambda t)}}xf(\eta), \quad \theta(\eta) = \frac{T - T_\infty}{T_w - T_\infty},$$

$$\phi(\eta) = \frac{C - C_\infty}{C_w - C_\infty}, \quad \zeta(\eta) = \frac{E - E_\infty}{E_w - E_\infty} \tag{8}$$

In view of the above similarity transformations of Equation (7), PDEs from (1)–(5) transform into the following system of nonlinear ODEs:

$$(1 + \frac{1}{\beta})f''' + ff'' - f'^2 - \sigma(\frac{\eta}{2}f'' + f') - Mf' + \lambda_1\theta + \lambda_2\phi + \lambda_3\zeta - k_p f' = 0, \tag{9}$$

$$(1 + R)\frac{1}{Pr}\theta'' - f'\theta + f\theta' - \sigma\left(\frac{\eta}{2}\theta' + 2\theta\right) + Nb\phi'\theta' + Nt\theta'^2 + Q\theta + N_d\phi'' = 0 \tag{10}$$

$$\frac{1}{Sc}\phi'' - f'\phi + f\phi' - \sigma\left(\frac{\eta}{2}\phi' + 2\phi\right) + S_r\theta'' = 0 \tag{11}$$

$$\zeta'' - Le\left[f'\zeta - f\zeta' + \sigma\left(\frac{\eta}{2}\zeta' + 2\zeta\right)\right] + \frac{Nt}{Nb}\theta'' = 0 \tag{12}$$

for the above problem the transformed boundary conditions are:

$$f(0) = f_w,$$

$$f'(0) = 1 + S_f f''(0), \tag{13}$$

$$\theta(0) = 1 + S_\theta \theta'(0), \tag{14}$$

$$\phi(0) = 1 + S_\phi \phi'(0), \tag{15}$$

$$\zeta(0) = 1 + S_\zeta \zeta'(0), \tag{16}$$

$$f'(\infty) \rightarrow 0, \theta(\infty) \rightarrow 0, \phi(\infty) \rightarrow 0, \zeta(\infty) \rightarrow 0, \tag{17}$$

where unsteadiness parameter  $\sigma = \lambda/a$ ,  $M$  is the magnetic field parameter,  $Pr$  is the Prandtl number,  $Nb$  is the Brownian motion parameter,  $Nt$  is the thermo-phoresis parameter,  $\beta$  is the Deborah number,  $Sc$  is the Schmidt number,  $R$  is the thermal radiation parameter,  $\lambda_1, \lambda_2$ , and  $\lambda_3$  are the buoyancy parameters,  $k_p$  is the permeability parameter,  $Nd$  is the Dufour parameter,  $Sr$  is the Soret parameter, and  $f_w$  is the Suction/injection parameter.

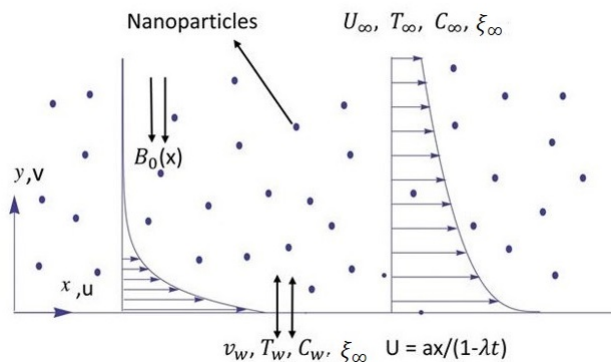


Figure 1. Physical sketch with xy-coordinates.

The primes show the differentiation with respect to  $\eta$ . The parameters used in Equations (8)–(11) are explained as:

$$M = \left[ \frac{\sigma(1-\lambda t)}{\rho a} B_0 \right]^{1/2}, Pr = \nu/\alpha, Nb = \tau D_B (C_w - C_\infty)/\nu, Nt = (\tau D_T (T_w - T_\infty))/\nu T_\infty, \beta = k_0 a / (1 - \lambda t), Sc = \frac{\nu}{D_m}, Le = \frac{\sigma}{D_B}, R = (16\sigma^* T_\infty^3)/(3k^* K), \sigma = \lambda/a, \lambda_1 = (g\beta_T T_0)/(2av), \lambda_2 = (g\beta_C C_0)/(2av), \lambda_3 = (g\beta_E E_0)/(2av), Sr = (D_T T_0)/\nu C_0, Nd = (D_m K_T C_0)/(C_s C_p T_0), k_p = \nu(1 - \lambda t)/a, f_w = -v_w(1 - \gamma t)^{1/2}/(\nu a)^{1/2},$$

Also, the local skin friction co-efficient, local Nusselt number, and local Sherwood number are explained as below

$$C_f = \frac{\mu}{\rho(U_w)^2} \left( \frac{\partial u}{\partial y} \right)_{y=0} \tag{18}$$

$$Nu = \frac{x}{k(T - T_\infty)} \left[ k \left( \frac{\partial T}{\partial y} \right)_{y=0} - \frac{4\sigma^*}{3k^*} \left( \frac{\partial T^4}{\partial y} \right)_{y=0} \right] \tag{19}$$

$$Sh = -\frac{x}{(C - C_\infty)} \left( \frac{\partial C}{\partial y} \right)_{y=0} \tag{20}$$

when Equation (7) is substituted into Equations (17)–(19), the final dimensionless form is obtained;  $C_{fr} = (Re_x)^{1/2} = f''(0)$ ,  $N_{ur} = Nu/(Re_x)^{1/2} = -(1 + R)\theta'(0)$ ,  $Shr = Sh/(Re_x)^{1/2} = -\phi'(0)$  where the local Reynolds number is  $Re_x$ , reduced skin friction is  $C_{fr}$ , reduced Nusselt number is  $N_{ur}$ , and the reduced Sherwood number is  $Shr$ .

### 3. Finite Element Method Solutions

We solve the system of non-linear boundary value problem that is given in Equations (8)–(11) numerically by applying the finite element method (FEM) subjected with the boundary conditions (12)–(16). The FEM is extremely effectual and has been applied to study different problems in fluid mechanics, CFD, mass transfer, heat transfer, solid mechanics, and also in many other fields. The general detail of the finite element method (FEM) can be found in Raddy [26–28]. Reddy [29] gives a general detail of the variational finite element method, which also found that the finite element method (FEM) is employed in commercial software like ADINA, ANSYS, MATLAB, and ABAQUS. Swapna et al. and Rana et al. [30,31] explain that the variational finite element method solves the boundary value problem very efficiently and accurately. To solve the non-linear boundary value problem (8)–(11) by using finite element method (FEM), along with boundary conditions (12)–(16), to apply FEM, first we have to consider:

$$f' = g. \tag{21}$$

The Equations (8)–(11) take the form

$$(1 + \frac{1}{\beta})g'' + fg' - g^2 - \sigma(\frac{\eta}{2}g' + g) - Mg + \lambda_1\theta + \lambda_2\phi + \lambda_3\zeta - k_p g = 0, \tag{22}$$

$$(1 + R)\frac{1}{Pr}\theta'' - g\theta + f\theta' - \sigma(\frac{\eta}{2}\theta' + 2\theta) + Nb\phi'\theta' + Nt\theta'^2 + Q\theta + N_d\phi'' = 0 \tag{23}$$

$$\frac{1}{Sc}\phi'' - g\phi + f\phi' - \sigma(\frac{\eta}{2}\phi' + 2\phi) + S_r\theta'' = 0 \tag{24}$$

$$\zeta'' - Le [g\zeta - f\zeta' + \sigma(\frac{\eta}{2}\zeta' + 2\zeta)] + \frac{Nt}{Nb}\theta'' = 0, \tag{25}$$

The corresponding boundary conditions now reduce to the following form:

$$f(0) = f_w, g(0) = 1 + S_f g'(0), \theta(0) = 1 + S_\theta \theta'(0), \phi(0) = 1 + S_\phi \phi'(0), \tag{26}$$

$$\zeta(0) = 1 + S_\zeta \zeta'(0), \tag{26}$$

$$h(\infty) \rightarrow 0, \theta(\infty) \rightarrow 0, \phi(\infty) \rightarrow 0, \zeta(\infty) \rightarrow 0, \tag{27}$$

#### 3.1. Variational Formulations

The variational formulation is associated with Equations (20)–(24) over a linear element  $(\eta_c, \eta_{c+1})$  is given by

$$\int_{\eta_c}^{\eta_{c+1}} w_1 \{f' - g\} d\eta = 0, \tag{28}$$

$$\int_{\eta_c}^{\eta_{c+1}} w_2 \{ (1 + \frac{1}{\beta})g'' + fg' - g^2 - \sigma(\frac{\eta}{2}g' + g) - Mg + \lambda_1\theta + \lambda_2\phi + \lambda_3\zeta - k_p g \} d\eta = 0, \tag{29}$$

$$\int_{\eta_c}^{\eta_{c+1}} w_3 \{ (1 + R)\frac{1}{Pr}\theta'' - g\theta + f\theta' - \sigma(\frac{\eta}{2}\theta' + 2\theta) + Nb\phi'\theta' + Nt\theta'^2 + Q\theta + N_d\phi'' \} d\eta = 0, \tag{30}$$

$$\int_{\eta_c}^{\eta_{c+1}} w_4 \{ \frac{1}{Sc}\phi'' - g\phi + f\phi' - \sigma(\frac{\eta}{2}\phi' + 2\phi) + S_r\theta'' \} d\eta = 0, \tag{31}$$

$$\int_{\eta_c}^{\eta_{c+1}} w_5 \{ \zeta'' - Le [g\zeta - f\zeta' + \sigma(\frac{\eta}{2}\zeta' + 2\zeta)] + \frac{Nt}{Nb}\theta'' \} d\eta = 0, \tag{32}$$

where  $w_1, w_2, w_3, w_4,$  and  $w_5$  are weight functions and maybe viewed as variations in  $f, g, \theta, \phi, \zeta$  resp.

### 3.2. Finite Element Formulations

The equation of finite element model that is gained from the Equations (27)–(31) by exchanging the FEM approximation in the form:

$$\bar{f} = \sum_{j=1}^3 \bar{f}_j^e \psi_j^e, \bar{g} = \sum_{j=1}^3 \bar{g}_j^e \psi_j^e, \bar{\theta}' = \sum_{j=1}^3 \bar{\theta}'_j^e \psi_j^e, \bar{\phi}' = \sum_{j=1}^3 \bar{\phi}'_j^e \psi_j^e \tag{33}$$

with  $w_1 = w_2 = w_3 = w_4 = w_5 = \psi_i^e (i = 1, 2, 3)$ , where the shape function  $\psi_i^e$  are the shape functions for the element  $(\eta_c, \eta_c + 1)$  and are taken as

$$\begin{aligned} \psi_1^e &= \frac{(\eta_{c+1}-\eta_c-2\eta)(\eta_{c+1}-\eta)}{(\eta_{c+1}-\eta_c)^2}, \psi_2^e = \frac{4(\eta-\eta_c)(\eta_{c+1}-\eta)}{(\eta_{c+1}-\eta_c)^2}, \\ \psi_3^e &= -\frac{(\eta_{c+1}-\eta_c-2\eta)(\eta-\eta_c)}{(\eta_{c+1}-\eta_c)^2}, \eta_c \leq \eta \leq \eta_{c+1}. \end{aligned} \tag{34}$$

Therefore, the finite element model equations are given by

$$\begin{bmatrix} [W^{11}] & [W^{12}] & [W^{13}] & [W^{14}] & [W^{15}] \\ [W^{21}] & [W^{22}] & [W^{23}] & [W^{24}] & [W^{25}] \\ [W^{31}] & [W^{32}] & [W^{33}] & [W^{34}] & [W^{35}] \\ [W^{41}] & [W^{42}] & [W^{43}] & [W^{44}] & [W^{45}] \\ [W^{51}] & [W^{52}] & [W^{53}] & [W^{54}] & [W^{55}] \end{bmatrix} \begin{bmatrix} f \\ g \\ \theta \\ \phi \\ \zeta \end{bmatrix} = \begin{bmatrix} b_1 \\ b_2 \\ b_3 \\ b_4 \\ b_5 \end{bmatrix} \tag{35}$$

where  $[W^{mn}]$  and  $b^m (m,n = 1,2,3,4,5)$  are the matrices and are given as:

$$\begin{aligned} [W_{ij}^{11}] &= \int_{\eta_c}^{\eta_{c+1}} \psi_i^e \frac{d\psi_j^e}{d\eta} d\eta, [W_{ij}^{12}] = - \int_{\eta_c}^{\eta_{c+1}} \psi_i^e \psi_j^e d\eta, [W_{ij}^{13}] = [W_{ij}^{14}] = 0, [W_{ij}^{15}] = [W_{ij}^{21}] = 0, \\ [W_{ij}^{22}] &= -(1 + \frac{1}{\beta}) \int_{\eta_c}^{\eta_{c+1}} \frac{d\psi_i^e}{d\eta} \frac{d\psi_j^e}{d\eta} d\eta + \int_{\eta_c}^{\eta_{c+1}} \bar{f} \psi_i^e \frac{d\psi_j^e}{d\eta} d\eta - \int_{\eta_c}^{\eta_{c+1}} \bar{g} \psi_i^e \psi_j^e d\eta - A \frac{\eta}{2} \int_{\eta_c}^{\eta_{c+1}} \psi_i^e \frac{d\psi_j^e}{d\eta} d\eta \\ &- \int_{\eta_c}^{\eta_{c+1}} \bar{g} \psi_i^e \psi_j^e d\eta - A \int_{\eta_c}^{\eta_{c+1}} \psi_i^e \psi_j^e d\eta - M \int_{\eta_c}^{\eta_{c+1}} \psi_i^e \psi_j^e d\eta - k_p \int_{\eta_c}^{\eta_{c+1}} \psi_i^e \psi_j^e d\eta \\ [W_{ij}^{23}] &= \lambda_1 \int_{\eta_c}^{\eta_{c+1}} \psi_i^e \psi_j^e d\eta, [W_{ij}^{24}] = \lambda_2 \int_{\eta_c}^{\eta_{c+1}} \psi_i^e \psi_j^e d\eta, [W_{ij}^{25}] = \lambda_3 \int_{\eta_c}^{\eta_{c+1}} \psi_i^e \psi_j^e d\eta, \\ [W_{ij}^{31}] &= 0, [W_{ij}^{32}] = 0, [W_{ij}^{33}] = -(1 + R) \frac{1}{Pr} \int_{\eta_c}^{\eta_{c+1}} \frac{d\psi_i^e}{d\eta} \frac{d\psi_j^e}{d\eta} d\eta - \int_{\eta_c}^{\eta_{c+1}} \bar{g} \psi_i^e \psi_j^e d\eta + \int_{\eta_c}^{\eta_{c+1}} \bar{f} \psi_i^e \frac{d\psi_j^e}{d\eta} d\eta \\ &- A \frac{\eta}{2} \int_{\eta_c}^{\eta_{c+1}} \psi_i^e \frac{d\psi_j^e}{d\eta} d\eta - 2A \int_{\eta_c}^{\eta_{c+1}} \psi_i^e \psi_j^e d\eta + Nb \int_{\eta_c}^{\eta_{c+1}} \bar{\phi}' \psi_i^e \frac{d\psi_j^e}{d\eta} d\eta \\ &+ Nt \int_{\eta_c}^{\eta_{c+1}} \bar{\theta}' \psi_i^e \frac{d\psi_j^e}{d\eta} d\eta + Q \int_{\eta_c}^{\eta_{c+1}} \psi_i^e \psi_j^e d\eta, [W_{ij}^{34}] = -Nd \int_{\eta_c}^{\eta_{c+1}} \frac{d\psi_i^e}{d\eta} \frac{d\psi_j^e}{d\eta} d\eta, [W_{ij}^{35}] = 0, \\ [W_{ij}^{41}] &= [W_{ij}^{42}] = 0, [W_{ij}^{43}] = -Sr \int_{\eta_c}^{\eta_{c+1}} \frac{d\psi_i^e}{d\eta} \frac{d\psi_j^e}{d\eta} d\eta, \\ [W_{ij}^{44}] &= -\frac{1}{Sc} \int_{\eta_c}^{\eta_{c+1}} \frac{d\psi_i^e}{d\eta} \frac{d\psi_j^e}{d\eta} d\eta + \int_{\eta_c}^{\eta_{c+1}} \bar{f} \psi_i^e \frac{d\psi_j^e}{d\eta} d\eta - \int_{\eta_c}^{\eta_{c+1}} \bar{g} \psi_i^e \psi_j^e d\eta d\eta \\ &- A \frac{\eta}{2} \int_{\eta_c}^{\eta_{c+1}} \psi_i^e \frac{d\psi_j^e}{d\eta} d\eta - 2A \int_{\eta_c}^{\eta_{c+1}} \psi_i^e \psi_j^e d\eta, \\ [W_{ij}^{45}] &= [W_{ij}^{51}] = [W_{ij}^{52}] = [W_{ij}^{54}] = 0, [W_{ij}^{53}] = -\frac{Nt}{Nb} \int_{\eta_c}^{\eta_{c+1}} \frac{d\psi_i^e}{d\eta} \frac{d\psi_j^e}{d\eta} d\eta \end{aligned}$$

$$\begin{aligned}
 [W_{ij}^{55}] &= - \int_{\eta_c}^{\eta_{c+1}} \frac{d\psi_i^e}{d\eta} \frac{d\psi_j^e}{d\eta} d\eta + Le \int_{\eta_c}^{\eta_{c+1}} \bar{f} \psi_i^e \frac{d\psi_j^e}{d\eta} d\eta - Le \int_{\eta_c}^{\eta_{c+1}} \bar{g} \psi_i^e \psi_j^e d\eta d\eta \\
 &- LeA \frac{\eta}{2} \int_{\eta_c}^{\eta_{c+1}} \psi_i^e \frac{d\psi_j^e}{d\eta} d\eta - 2LeA \int_{\eta_c}^{\eta_{c+1}} \psi_i^e \psi_j^e d\eta,
 \end{aligned}
 \tag{36}$$

and

$$\begin{aligned}
 b_i^1 &= 0, b_i^2 = -(\psi \frac{dg}{d\eta})_{\eta_c}^{\eta_{c+1}}, b_i^3 = -(1 + R) \frac{1}{Pr} (\psi \frac{d\theta}{d\eta})_{\eta_c}^{\eta_{c+1}} - Nd (\psi \frac{d\phi}{d\eta})_{\eta_c}^{\eta_{c+1}}, \\
 b_i^4 &= -\frac{1}{Sc} (\psi \frac{d\phi}{d\eta})_{\eta_c}^{\eta_{c+1}} - Sr (\psi \frac{d\theta}{d\eta})_{\eta_c}^{\eta_{c+1}}, b_i^5 = -(\psi \frac{d\xi}{d\eta})_{\eta_c}^{\eta_{c+1}} - \frac{Nt}{Nb} (\psi \frac{d\theta}{d\eta})_{\eta_c}^{\eta_{c+1}},
 \end{aligned}$$

where  $\bar{f} = \sum_{j=1}^3 \bar{f}_j \psi_j^e$ ,  $\bar{g} = \sum_{j=1}^3 \bar{g}_j \psi_j^e$ ,  $\bar{\theta}' = \sum_{j=1}^3 \bar{\theta}'_j \psi_j^e$ , and  $\bar{\phi}' = \sum_{j=1}^3 \bar{\phi}'_j \psi_j^e$  are assumed to be known.

After the assemblage of element equations, a consequential system of non-linear equations is obtained, after that, it requires an iterative scheme to solve it for an efficient solution. The calculation of  $f, g, \theta$ , and  $\phi$  are then conceded out for a higher level, and then proceeding until the required 0.00005 is not obtained. The results in Table 1 show the convergency, as we computed, for the increasing number of elements,  $n = 300, 500, 1000, 1300, 1500, 1800, 1900, 2100$ . From the results, it is clear that as the number of elements increases further, no significant difference in the values of  $f, g, \theta, \phi$ , and  $\xi$  can be seen as the number of elements increases beyond 1800, so the outcomes at  $n = 1800$  elements are reported.

**Table 1.** The convergence of the results of finite element method (FEM) when  $Pr = 1, M = \sigma = 0.2, \beta = 0.1, \lambda_1 = \lambda_2 = \lambda_3 = 0.2, S_f = S_\theta = S_\phi = S_\xi = S_t = Sr = R = S_g = S_p = 0.5, kp = Nu = Nt = Nb = 0.1, Sc = 10, Le = 5, f_w = 0.3$ .

Number of Elements	$f(3)$	$g(3)$	$\theta(3)$	$\phi(3)$	$\xi(3)$
300	0.82439	0.16241	0.16733	0.06876	0.03046
500	0.82455	0.16250	0.19729	0.06875	0.03046
1000	0.82466	0.16257	0.19726	0.06874	0.03045
1300	0.82469	0.16259	0.19726	0.06873	0.03045
1500	0.82470	0.16260	0.19725	0.06873	0.03045
1800	0.82471	0.16260	0.19725	0.06873	0.03045
1900	0.82472	0.16261	0.19725	0.06874	0.03045
2100	0.82472	0.16261	0.19725	0.06874	0.03045

#### 4. Results and Discussion

The numerical calculations have been performed for the velocity, temperature, solutal, and Casson nano-fluid volume fraction functions for a different assessment of physical parameters, as magnetic parametre  $M$ , Prandtl number  $Pr$ , Unsteadiness  $\sigma$ , permeability  $k_p$ , Brownian motion  $Nb$ , thermophoresis  $Nt$ , thermal radiation  $R$ , Dufour  $Nd$ , Schmidt  $Sc$ , buoyancy  $\lambda_1, \lambda_2, \lambda_3$ , Suction/Injection  $f_w$ , Soret  $Sr$ , Lewis number  $Le$ , hydro-dynamic slip  $S_f$ , thermal slip  $S_\theta$ , solutal slip  $S_\phi$ , and nano-particles concentration slip  $S_\xi$ .

The detail of the present results and the appraisal of flow velocity is made with the exact solution that is given by Crane [32] as  $f(\eta) = 1 - e^{(-\eta)}$  under the special case ( $M = 0, \sigma = 0, \beta \rightarrow \infty, \lambda_1 = \lambda_2 = \lambda_3 = 0, S_f = 0, f_w = 0, kp = 0$ ). The finite element method's outcomes have decent concurrence with the exact solution, which approves the validity of the finite element method. It can be seen clearly in Table 2, and in Table 3, that the skin friction coefficient attained by the finite element method is equivalent to the numerical outcomes of Giressha et al. [33] and the exact solution of Mudassar et al. [34] under special case  $\sigma = 0, \beta = 0, \lambda_1 = \lambda_2 = \lambda_3 = 0, S_f = 0, f_w = 0, kp = 0$ . To confirm the accuracy of the presented numerical results, the results obtained by the finite element method for skin friction co-efficient for steady and unsteady flow have been compared with the numerical results that have previously been reported in studies and shown in Table 4. Regarding our

results, there is admirable conformity among our outcomes and previously available research articles, which approves the cogency and the accuracy of the current results that are obtained by the finite element method (FEM). Table 5 describes the results of the heat transfer rate that are acquired by the finite element method, which are compared with the results of earlier studies and with the accurate solution of Ishak et al. [35] in a special case ( $Nt = Nb = 0$ ). We observe that our results are in complete agreement and the grid invariance test has performed to sustain accuracy for 4 decimal points. In Table 6, local skin friction coefficient  $-f''(0)$ , the rates of heat transfer  $-\theta'(0)$ , and mass transfer  $-\phi'(0)$  that are acquired by FEM, which are also compared with the published research work, show excellent correlation.

**Table 2.** The comparison of the exact solution of Crane and FEM for the flow velocity  $f'(\eta)$ .

$\eta$	Crane [32]	FEM	$\eta$	Crane [32]	FEM
0	1	1	7	0.0009	0.0009
1	0.1379	0.1379	8	0.0003	0.0003
2	0.1353	0.1353	9	0.0001	0.0001
3	0.0498	0.0498	10	0.0000	0.0000
4	0.0183	0.0018	11	0.0000	0.0000
5	0.0067	0.0067	12	0.0000	0.0000
6	0.0025	0.0025	13	0.0000	0.0000

**Table 3.** Assessment of skin friction coefficient for different values of M.

M	Gireesha et al. [33]	Mudassar et al. [34]	FEM (Our Results)		Error in %
	$\beta = 0$	Exact Solution (a)	(b)		$ (\frac{b-a}{a})  \times 100$
0.0	1.000	1.000000	1.0000078		0.00078
0.2	1.095	1.095445	1.0954462		0.00010
0.5	1.224	1.224745	1.2247452		0.00001
1.0	1.414	1.414214	1.4142142		0.00001
1.2	1.483	1.483240	1.4832385		0.00010
1.5	1.581	1.581139	1.5811392		0.00001
2.0	1.732	1.732051	1.7320515		0.00002

**Table 4.** Assessment of skin friction coefficient for various values of M and  $\sigma$  when  $f_w = \lambda_1 = \lambda_2 = \lambda_3 = k_p = S_f = 0$ .

M	Mabood and Das [36]	Fazle and Stanford [25]	FEM (Our Results)	$\sigma$	Chamkha et al. [37]	Fazle and Stanford [25]	FEM (Our Results)
0	-1.000008	-1.0000084	-1.0000082	0.2	-	-	1.068027
1	1.4142135	1.41421356	1.41421353	0.4	-	-	1.134687
5	2.4494897	2.44948974	2.44948963	0.6	-	-	1.199118
10	3.3166247	3.31662479	3.31662463	0.8	1.261512	1.261042	1.261042
50	7.1414284	7.14142843	7.14142839	1.0	-	-	1.320522
100	10.049875	10.0498756	10.0498751	1.2	1.378052	1.377724	1.377724
500	22.383029	22.3830293	22.3830283	1.4	-	-	1.432836
1000	31.638584	31.6385840	31.6385833	1.6	-	-	1.486039

**Table 5.** Comparison of  $-\theta'(0)$  for various values of Pr when  $M = f_w = S_\theta = \sigma = \lambda_1 = \lambda_2 = \lambda_3 = R = Nd = k_p = S_f = 0$ .

Pr	Ali [38]	Fazle and Stanford [25]	Ishak et al. [35]	Dulal Pal. [39]	Haile et al. [40]	Ishak et al. [35] (a) Exact Solution	FEM (b) Our Results	Error in % $ (\frac{b-a}{a})  \times 100$
0.72	0.8058	0.8088	-	-	-	0.8086313498	0.8086339299	0.0003
1.00	0.9691	1.0000	1.0000	1.0000	1.0004	1.0000000000	1.0000080213	0.0008
3.00	1.9144	1.9237	1.9237	1.9236	1.9234	1.923682594	1.9236777221	0.0003
10.0	3.7006	3.7207	3.7207	3.7207	3.7205	3.720673901	3.7206681683	0.0002
100	-	-	12.2941	12.2940	12.2962	12.294083260	12.294051659	0.0003

**Table 6.** Comparison of  $-f''(0)$ ,  $-\theta'(0)$ , and  $-\phi'(0)$  for different values of Pr, and Sc when  $M = \sigma = \lambda_3 = \beta = R = Nb = Nt = Nd = Sr = 0, f_w = 0.5, \lambda_1 = k_p = 1, \lambda_2 = 2, S_f = S_\theta = S_\phi = S_\zeta = 0$ .

Pr	Sc	Chamkha et al. [37]			FEM(Our Results)		
		$-f''(0)$ ,	$-\theta'(0)$ ,	$-\phi'(0)$	$-f''(0)$	$-\theta'(0)$	$-\phi'(0)$
0.71	0.22	0.27377	1.158393	0.740140	0.27371	1.158389	0.740160
	0.60	0.49677	1.101087	1.312248	0.49669	1.101082	1.312192
	0.94	0.59941	1.076931	1.713443	0.59935	1.076899	1.713358
0.3	0.62	0.38639	0.621980	1.355045	0.38655	0.621892	1.355036
0.71		0.50438	1.099032	1.337571	0.50429	1.099018	1.337267
1.0		0.55244	1.384875	1.331027	0.55237	1.384753	1.331856
3.0		0.69042	2.966999	1.316710	0.69036	2.966894	1.316382

Figure 2 shows the effect of  $M$  on the velocity function with no hydro-dynamic slip and with hydro-dynamic slip. The results show that in both cases the velocity component decreases as the value of the magnetic parameter  $M$  increases. Physically, the magnetic parameter  $M$  produced Lorentz force like a drag force, which causes the motion of the fluid to decelerate. Figure 2 also shows that in both cases the suction  $f_w$  decelerates the momentum boundary layer thickness. The boundary layer thickness can be controlled with the help of suction  $f_w$ .

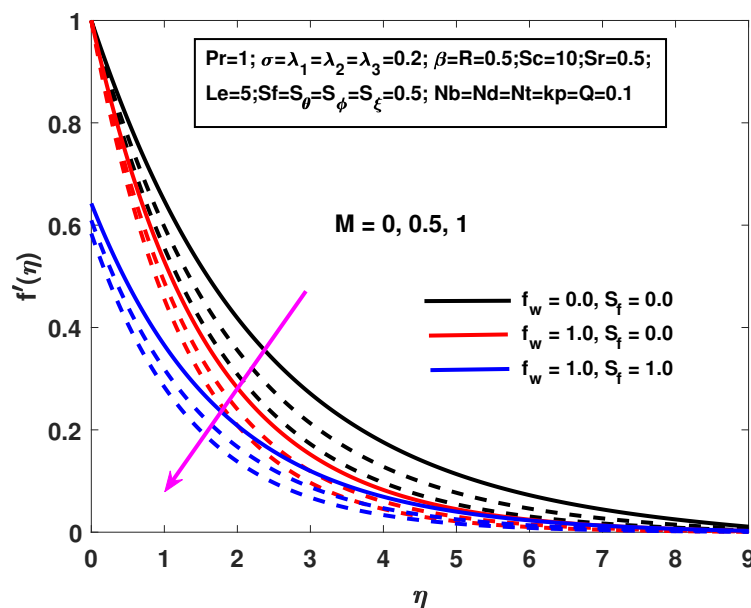


**Figure 2.** Effects of  $M, f_w$ , and  $S_f$  on  $f'$ .

Figures 3 and 4 exemplify that the velocity boundary layer thickness increases with enhancing the thermal buoyancy parameter  $\lambda_1$  and the nano-particles concentration buoyancy parameter  $\lambda_3$  in the non-existence of hydro-dynamic slip and the existence of hydro-dynamic slip. In these two cases, we have to perceive that the momentum boundary layer is prolonged with the increasing values of buoyancy  $\lambda_1$  and  $\lambda_3$ . Also in Figures 3 and 4, the velocity profile is increasing in the case of steady and unsteady flow and alike behavior of solutal buoyancy has been observed in Figure 5. It is observed that increasing the value of radiation parameter  $R$  is the reason to improve the velocity profile and incentive of instability in parameter  $k_p$ , and the velocity profile is explained in Figure 6.

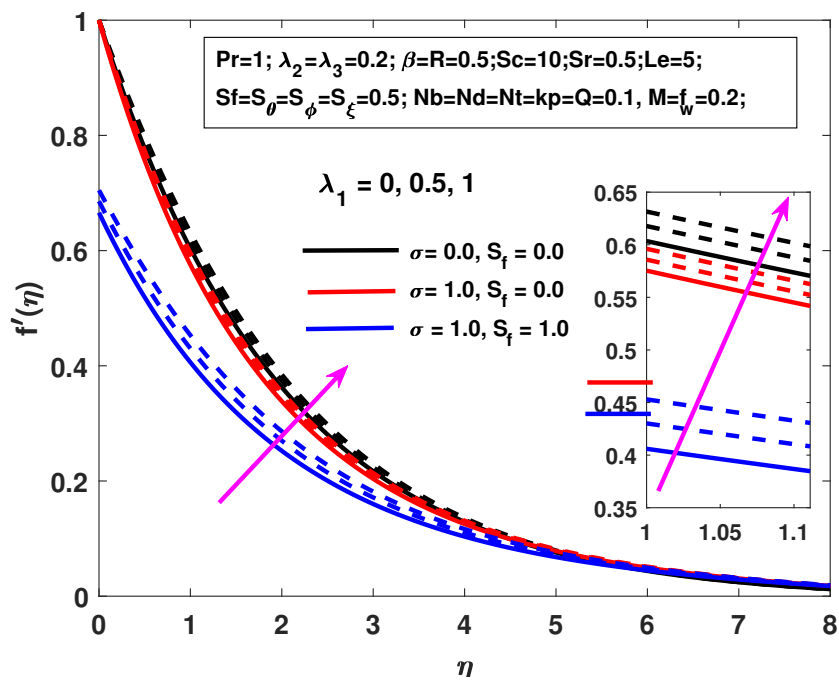


Figure 3. Effects of  $\lambda_1, \sigma$ , and  $S_f = 0$  on  $f'$ .

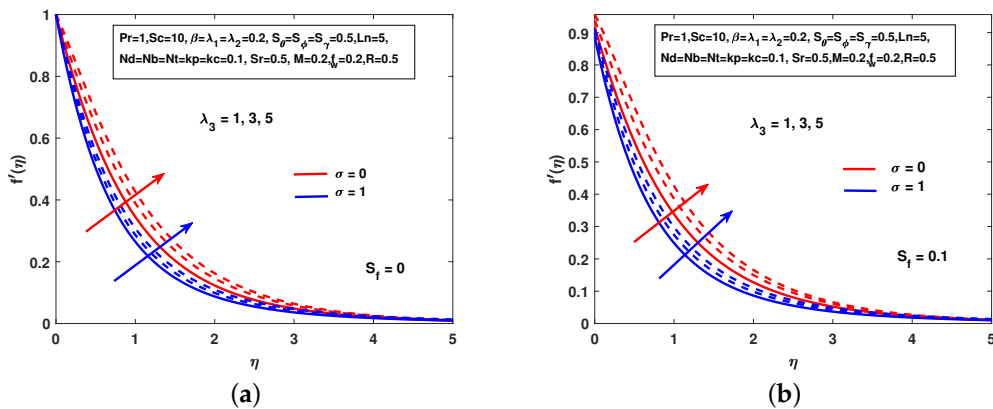


Figure 4. Effects of  $\lambda_3$  and  $\sigma$  on  $f'$ . (a)  $S_f = 0$  (b)  $S_f = 0.1$ .

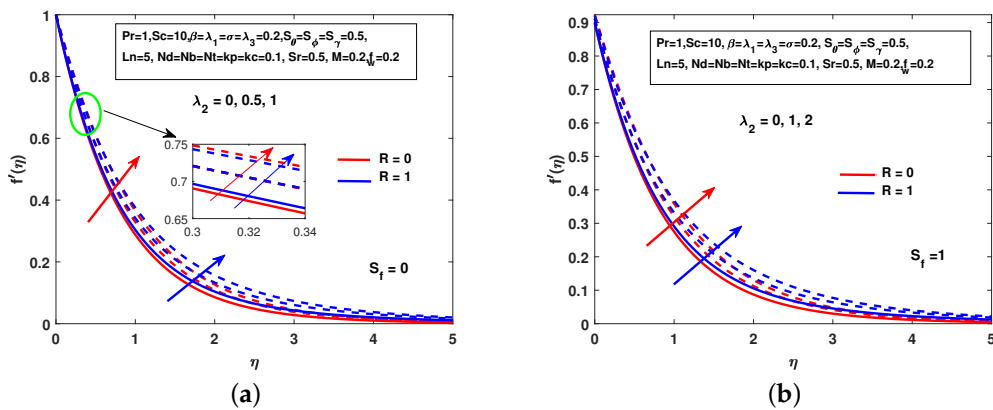


Figure 5. Effects of  $\lambda_2$  and  $R$  on  $f'$ . (a)  $S_f = 0$  (b)  $S_f = 1$ .

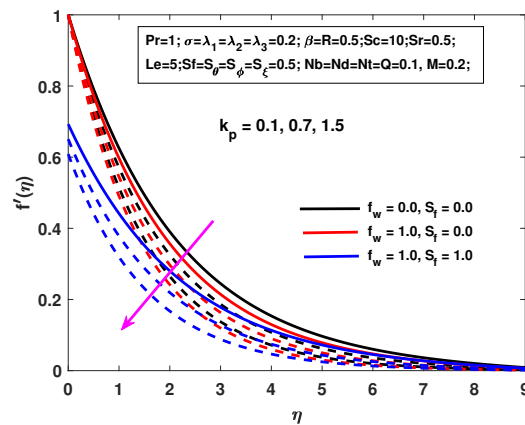


Figure 6. Effects of  $k_p$ ,  $f_w$ , and  $S_f$  on  $f'$ .

Also, we perceive in both cases that as the permeability of  $k_p$  increases, this causes a decline in the velocity profile with no hydro-dynamic slip and with hydro-dynamic slip. Furthermore, we also perceive in Figure 6 that the suction decreases the momentum boundary layer thickness. Similar behavior of the Deborah number  $\beta$  has been perceived on the velocity profile in Figure 7. Figure 8 indicates the impact of  $M$  on the temperature profile with the non-existence of thermal slip and with existence thermal slip. In the figure, it is clear that with an increasing value of  $M$  the temperature profile also increases in both cases. From Figure 8 it is also clear that suction  $f_w$  decreases the thermal boundary layer thickness in both cases and the thickness of the thermal boundary layer can be controlled with the help of suction  $f_w$ . Figure 9 depicts the similar behavior of  $M$ . It is perceived that the temperature increases with the discrepancy in parameter  $R$ .

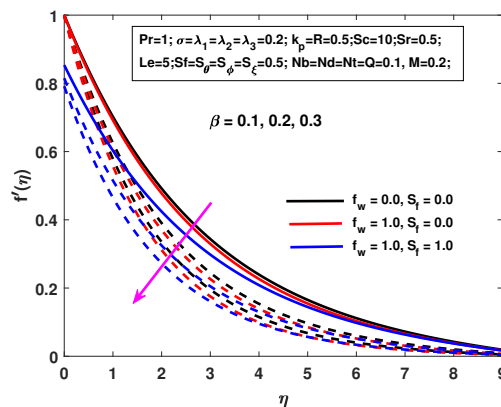


Figure 7. Effects of  $\beta$ ,  $f_w$ , and  $S_f$  on  $f'$ .

Figure 10 demonstrates the influence of  $\sigma$  and  $Pr$  on the temperature profile with and without the existence of thermal slip, with increasing  $Pr$ ,  $\sigma$ , and  $S_\theta$  causing the thermal boundary layer to decrease. The description of the effect of  $N_b$ ,  $f_w$ , and  $S_\theta$  with the temperature profile is explained in Figure 11. It is clear that with the increase in  $N_b$ , the thermal boundary layer of fluid flow increases in both cases. It can also be perceived that  $f_w$  decreases the thermal boundary layer thickness in both cases. In Figure 12, there is the influence of  $M$  and  $Sc$  on the solutal profile with the non-existence of solutal slip and with the existence of solutal slip. From the figure, it is clear that with the increasing value of  $M$ , the solutal profile also increases in both cases. Furthermore, the effect of  $S_c$  over the solutal profile declines the profile. The impact of the existence and non-existence of solutal slip and increasing values of  $S_r$  is depicted in Figure 13. It is seen that increasing the value of the Soret parameter increases the solutal profile in both the steady and unsteady cases. It is also seen that increasing the value of the slip results in decreasing the thickness of the solutal profile boundary.

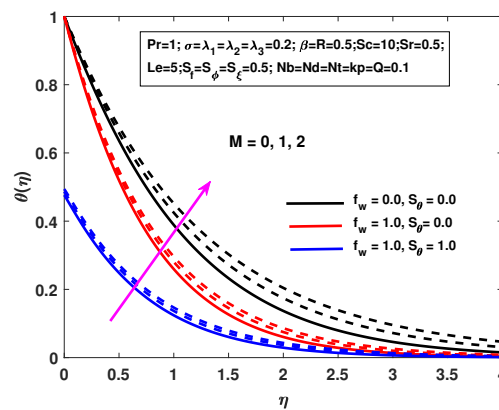


Figure 8. Effects of  $M$ ,  $f_w$ , and  $S_\theta$  on  $\theta$ .

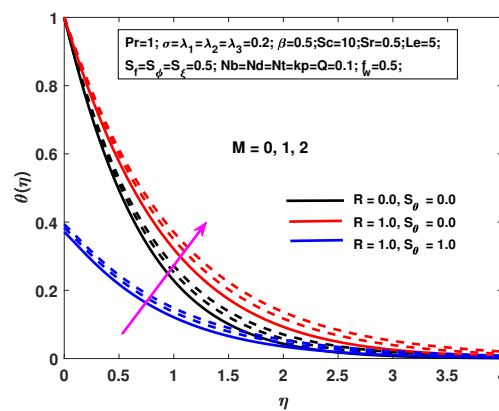


Figure 9. Effects of  $M$ ,  $R$ , and  $S_\theta$  on  $\theta$ .

Figure 14 indicates the impact of  $N_t$  on the nano-particle volume fraction profile without the existence of nano-particles concentration slip and with the existence of nano-particles concentration slip. It is clear from the figure that in both the steady and unsteady cases, increasing values of  $N_t$  cause a decline in the nano-particle volume fraction profile. The impacts of  $\sigma$  and  $S_\gamma$  over the nano-particle volume fraction profile have been illustrated in Figure 14. It is noticed that the nano-particle volume fraction profile decreases in increments in the values of  $\sigma$  and  $S_\gamma$ . Figures 15 and 16 show the impact of Lewis number  $Le$ , unsteadiness parameter  $\sigma$ , and suction parameter  $f_w$  on the nano-particle volume fraction profile, and interpretations about the nano-particle volume fraction profile are made. It is seen that increasing values of  $Le$  and  $f_w$  in the boundary layer of nano-particles causes the volume fraction profile to decline. In addition, it is clear from the figures that the nano-particle volume fraction profile decreases both with and without the existence of nano-particles concentration slip.

Figure 17 shows the impact of  $M$ ,  $\sigma$ , and  $S_f$  on the skin friction co-efficient and also shows that the skin friction co-efficient decreases with the increase of slip parameter, magnetic and unsteadiness parameter. In Figure 18, the skin friction coefficient increases with the increment in the thermal buoyancy, suction parameters, and solutal buoyancy. Figure 19 represents the increment in the value of Nusselt number with increasing values of magnetic, radiation and thermal slip parameters. As perceive in Figure 20 that when the values of solutal buoyancy and suction intensity increases with the existence and the non-existence absence of thermal buoyancy. Figure 21 demonstrates that the impact of  $Sc$ ,  $Sr$ , and  $S_\phi$  on the reduced Sherwood number. Also from the Figure 22, it clear that the reduced Sherwood number decreases with increment in the values of the unsteadiness parameter  $\sigma$ , magnetic parameter  $M$  and the suction parameters  $f_w$ .

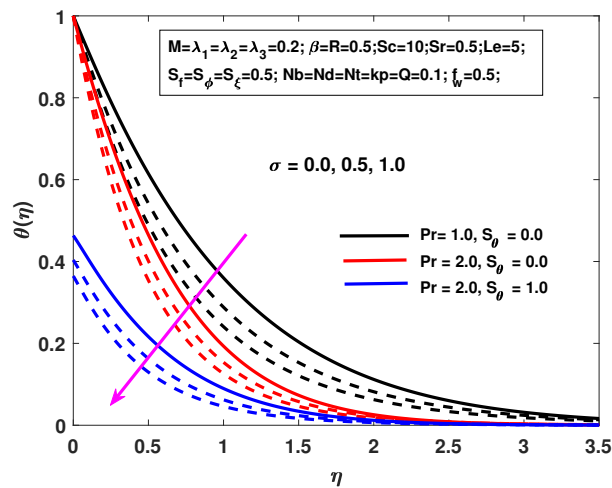


Figure 10. Effects of  $\sigma$ ,  $Pr$ , and  $S_\theta$  on  $\theta$ .

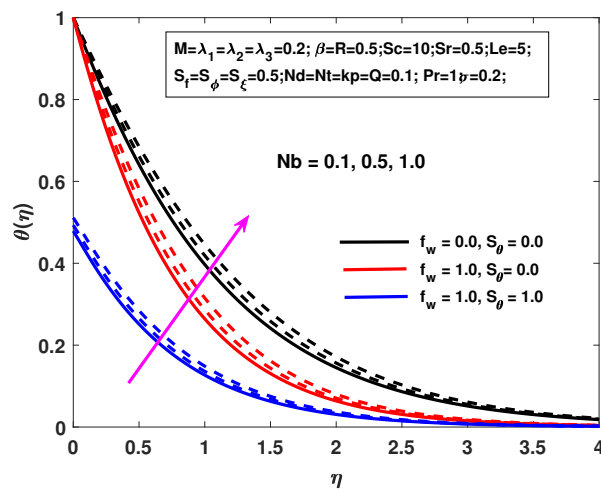


Figure 11. Effects of  $Nb$ ,  $f_w$ , and  $S_\theta$  on  $\theta$ .

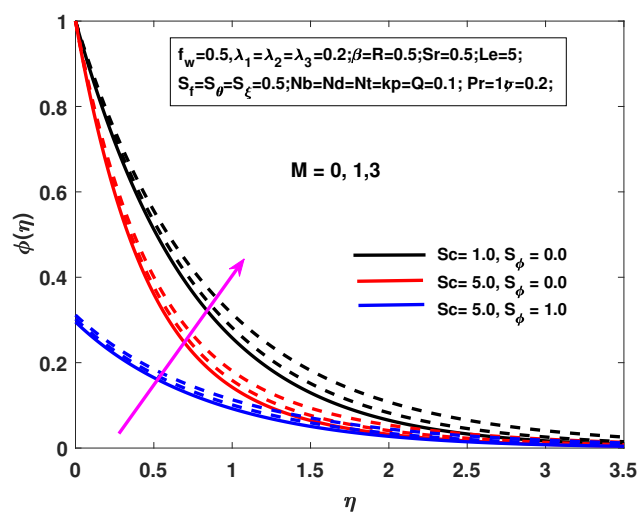


Figure 12. Effects of  $M$ ,  $Sc$ , and  $S_\phi$  on  $\phi$ .

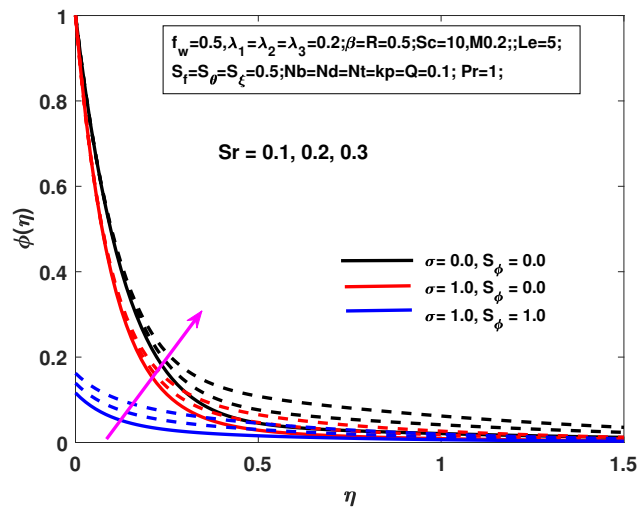


Figure 13. Effects of  $Sr$ ,  $\sigma$ , and  $S_\phi$  on  $\phi$ .

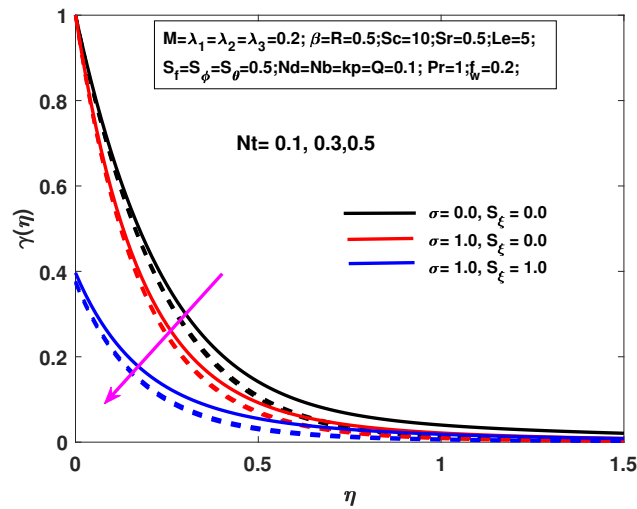


Figure 14. Effects of  $Nt$ ,  $\sigma$ , and  $S_\xi$  on  $\xi$ .

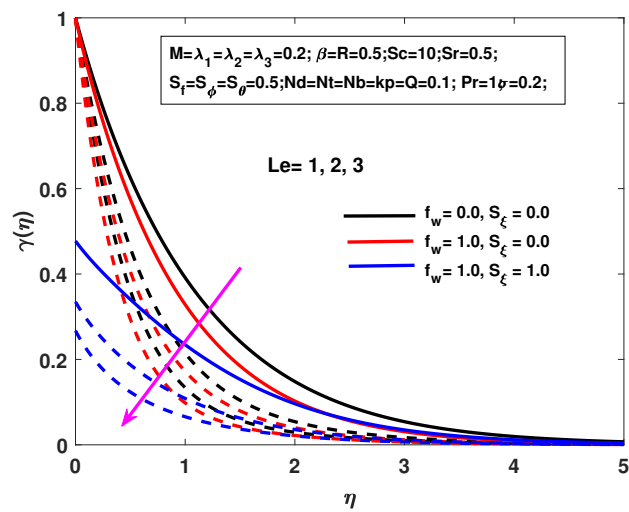


Figure 15. Effects of  $Le$ ,  $f_w$ , and  $S_\xi$  on  $\xi$ .

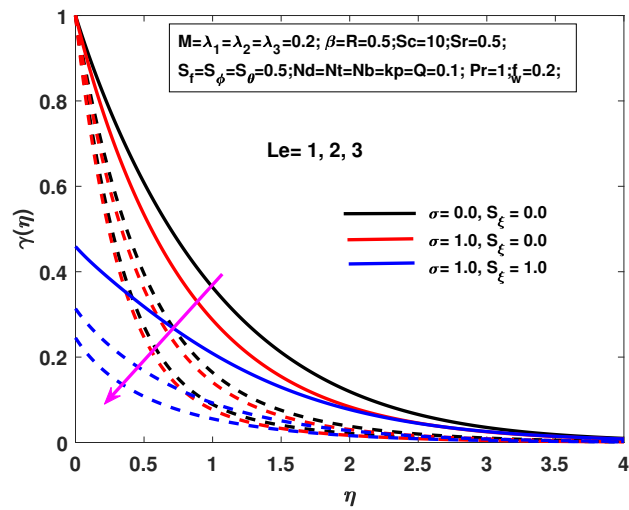


Figure 16. Effects of  $Le$ ,  $\sigma$ , and  $S_{\zeta}$  on  $\zeta$ .

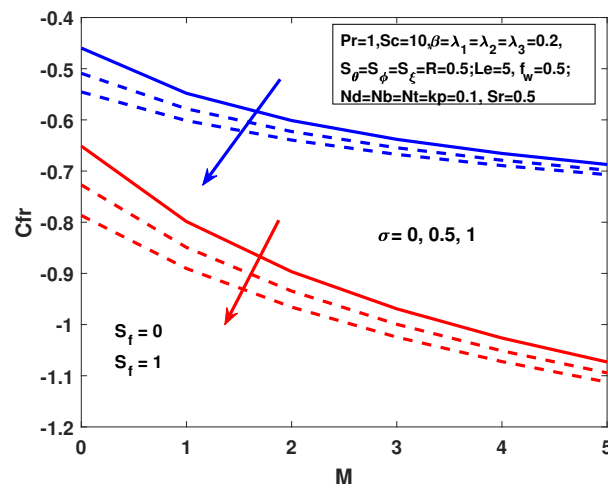


Figure 17. Effects of  $M$ ,  $\sigma$ , and  $S_f$  on the skin friction coefficient.

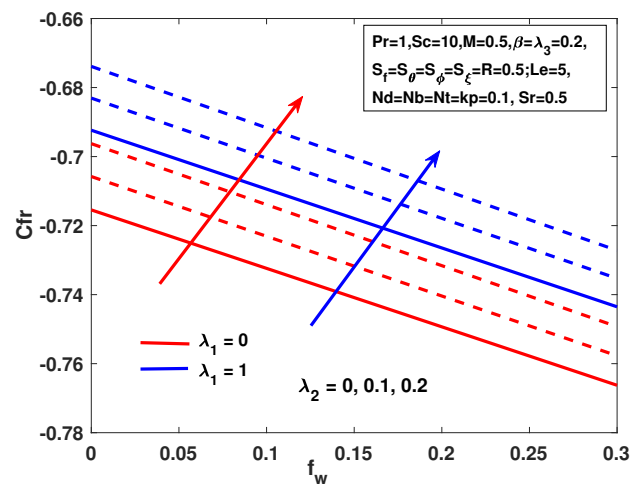


Figure 18. Effects of  $f_w$ ,  $\lambda_1$ , and  $\lambda_2$  on the skin friction coefficient.

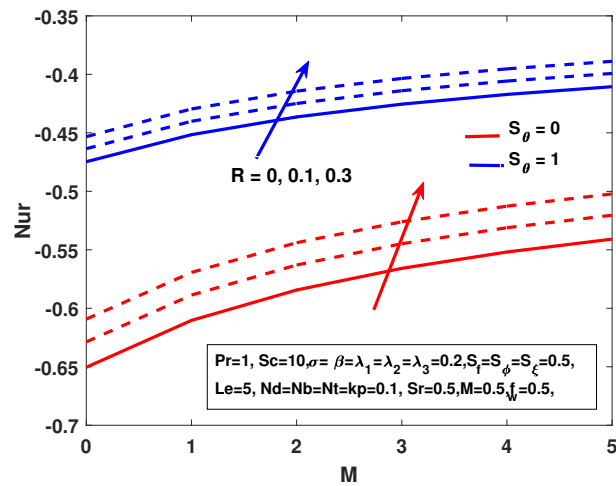


Figure 19. Effects of  $M$ ,  $R$ , and  $S_\theta$  on the reduced nusselt number.

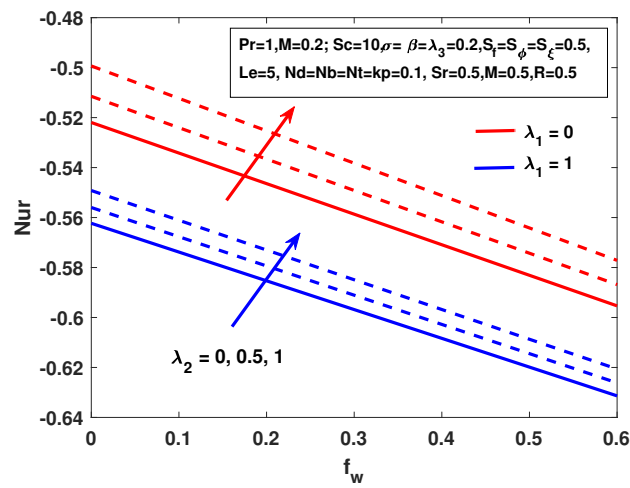


Figure 20. Effects of  $f_w$ ,  $\lambda_1$ , and  $\lambda_2$  on the reduced nusselt number.

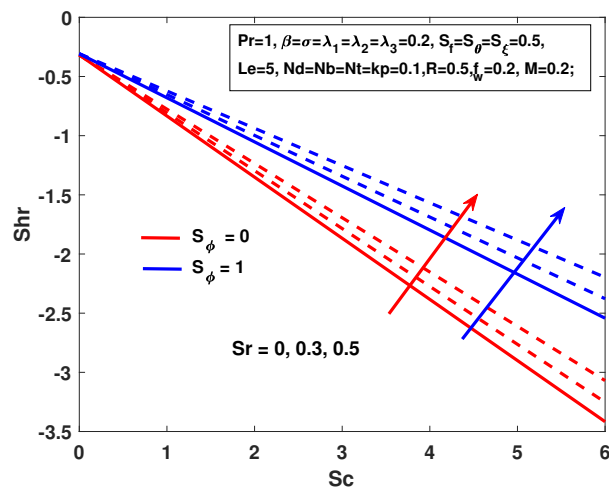


Figure 21. Effects of  $Sc$ ,  $Sr$ , and  $S_\phi$  on the reduced Sherwood number.

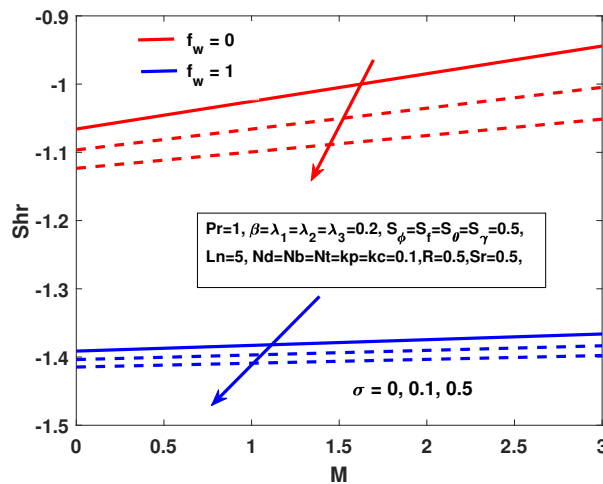


Figure 22. Effects of  $M$ ,  $\sigma$ , and  $f_w$  on the reduced Sherwood number.

In Table 7 we analyze the variation of physical parameters  $M, \lambda_1, \lambda_2, \lambda_3, \sigma, Pr, Le$  on skin friction co-efficient  $-f''(0)$ , Nusselt number  $-\theta'(0)$ , and Sherwood number  $-\zeta'(0)$ .

The following results are concluded from Table 7:

- (i) The skin-friction coefficient is increasing while reducing the local Nusselt and Sherwood numbers through improvement in the Magnetic parameter;
- (ii) The increment in thermal buoyancy parameters  $\lambda_1, \lambda_2, \lambda_3$  causes the skin-friction coefficient to decrease while increasing the local Nusselt number and Sherwood number;
- (iii) With the increasing unsteadiness parameter  $\sigma$ , the skin-friction coefficient, local Nusselt, and Sherwood numbers are also increasing;
- (iv) The skin-friction coefficient is increasing with the increment in Prandtl number and the local Nusselt number and Sherwood number also increase;
- (v) The skin-friction coefficient is increasing with the increasing Lewis number and also increment in the local Nusselt number and Sherwood number.

Table 7. Various mathematical values of physical constraints  $M, \lambda_1, \lambda_2, \lambda_3, \sigma, Pr, Le$  when  $R = f_w = S_r = S_t = S_f = S_p = S_g = 0.5, k_p = 0.1, N_u = N_b = N_t = Q = 0.1, \beta = 0.2, S_c = 10$ .

M	$\lambda_1$	$\lambda_2$	$\lambda_3$	$\sigma$	Pr	Le	$-f''(0)$	$-\theta'(0)$	$-\zeta'(0)$
0.5	0.2	0.2	0.2	0.5	1	5	0.43564	0.70863	1.33066
1.0							0.47695	0.70192	1.32746
1.5							0.51239	0.69612	1.32468
0.5	0.2	0.2	0.2	0.5	1	5	0.43564	0.70863	1.33066
							0.42223	0.71052	1.33163
							0.40901	0.71237	1.33258
0.5	0.2	0.2	0.2	0.5	1	5	0.43564	0.70863	1.33066
							0.43095	0.70928	1.33099
							0.42628	0.70993	1.33133
0.5	0.2	0.2	0.2	0.5	1	5	0.43564	0.70863	1.33066
							0.43217	0.70906	1.33089
							0.42870	0.70949	1.33113
0.5	0.2	0.2	0.2	0.5	1	5	0.43564	0.70863	1.33066
							0.46926	0.79556	1.37699
							0.49903	0.86094	1.41349
0.5	0.2	0.2	0.2	0.5	1	5	0.43564	0.70863	1.33066
							0.43819	0.88813	1.28962
							0.43925	1.00288	1.25652
0.5	0.2	0.2	0.2	0.5	1	5	0.43564	0.70863	1.33066
							0.43635	0.70919	1.44132
							0.43689	0.70993	1.54699

## 5. Conclusions

In this paper, we have developed a mathematical model to investigate the unsteady two-dimensional magnetohydrodynamic (MHD) flow and heat transfer of an incompressible electrically conducted fluid. This study was conducted to analyze the multiple slip effects on magneto-hydrodynamic unsteady Casson nano-fluid flow over a non-linear porous shrinking/stretching sheet in the presence of a heat source with Soret effect. Appropriate similarities have been used for transformations and the governing partial differential equations (PDEs) are rendered into a system of ordinary differential equations (ODEs). The resulting system of ordinary differential equations was solved numerically with an efficient and validated finite element method (FEM). We also use a special case of the present model to compare our results with previous studies. A parametric study has been performed to explore the mass and heat transfer characteristics, and also the impact of different parameters, of the flow. The following are the results that can be concluded from the present study.

- The cause of reducing the fluid velocity near the region of the boundary layer is the increment in values of slip, suction, magnetic field, and unsteady parameters.
- The increment in thermal buoyancy parameters  $\lambda_1, \lambda_2, \lambda_3$  and slip parameters cause decreasing the skin-friction coefficient while increasing the local Nusselt number and Sherwood number.
- Decreasing the value of the Sherwood number causes an increasing value of the solutal slip parameter, Schmidt number, and Soret number, but the effect is the opposite with increasing values of the unsteadiness, magnetic, and suction parameters.
- With the increasing value of the magnetic parameter  $M$ , the slip velocity parameter and suction parameter are found to be reduced in the velocity profile.
- The skin-friction coefficient decreases with the increasing value of slip, magnetic, and unsteadiness parameters, but the effect is the opposite for increasing values of thermal buoyancy, suction parameter, and solutal buoyancy.
- The increment of the values of buoyancy parameter, injection parameter, and heat source parameter cause an increase in the velocity profile.

**Author Contributions:** L.A. modeled the problem and wrote the manuscript. X.L. thoroughly checked the mathematical modeling and English corrections. B.A. helped in MATLAB coding. S.M., and S.A. writing—review and editing. X.L. contributed to the results and discussions. All authors finalized the manuscript after its internal evaluation.

**Funding:** This work was supported by the National Natural Science Foundation of China (No. 51676152), Equipment Advance Research Field Foundation (No. 61402070302), and Fundamental Research Funds for the Central Universities (No. zrzdz2017012).

**Acknowledgments:** The first author acknowledge with thanks the Liu Xiaomin for his continuous guidance throughout the work at Xian Jiaotong University China, National Natural Science Foundation of China, Equipment Advance Research Field Foundation, Fundamental Research Funds for the Central Universities for technical and financial support for this research project. Authors would also like to acknowledge and express their gratitude to the Chinese Government Scholarship Council (CSC) for the scholarship award.

**Conflicts of Interest:** The authors declare no conflict of interest.

## References

1. Tretheway, D.C.; Meinhart, C.D. Apparent fluid slip at hydrophobic microchannel walls. *Phys. Fluids* **2002**, *14*, L9–L12. [[CrossRef](#)]
2. Soltani, F.; Yilmazer, L. Slip velocity and slip layer thickness in flow of concentrated suspensions. *J. Appl. Polym. Sci.* **2010**, *70*, 515–522. [[CrossRef](#)]
3. Mabood, F.; Das, K. Melting heat transfer on hydromagnetic flow of a nanofluid over a stretching sheet with radiation and second-order slip. *Eur. Phys. J. Plus* **2016**, *131*, 1–12. [[CrossRef](#)]
4. Pop, I.; Na, T.Y. Unsteady flow past a stretching sheet. *Mech. Res. Commun.* **1996**, *23*, 413–422. [[CrossRef](#)]
5. Sharidan, S.; Mahmood, M.; Pop, I. Similarity solutions for the unsteady boundary layer flow and heat transfer due to a stretching sheet. *Appl. Mech. Eng.* **2006**, *11*, 647.

6. Bhattacharyya, K.; Mukhopadhyay, S.; Layek, G. Slip effects on an unsteady boundary layer stagnation-point flow and heat transfer towards a stretching sheet. *Chin. Phys. Lett.* **2011**, *28*, 094702. [[CrossRef](#)]
7. Khan, U.; Ahmed, N.; Mohyud-Din, S.T. Heat transfer effects on carbon nanotubes suspended nanofluid flow in a channel with non-parallel walls under the effect of velocity slip boundary condition: A numerical study. *Neural Comput. Appl.* **2017**, *28*, 37–46. [[CrossRef](#)]
8. Mohyud-Din, S.T.; Zaidi, Z.A.; Khan, U.; Ahmed, N. On heat and mass transfer analysis for the flow of a nanofluid between rotating parallel plates. *Aerosp. Sci. Technol.* **2015**, *46*, 514–522. [[CrossRef](#)]
9. Mohyud-Din, S.; Khan, U.; Ahmed, N.; Hassan, S. Magnetohydrodynamic flow and heat transfer of nanofluids in stretchable convergent/divergent channels. *Appl. Sci.* **2015**, *5*, 1639–1664. [[CrossRef](#)]
10. Makinde, O.; Mishra, S. On stagnation point flow of variable viscosity nanofluids past a stretching surface with radiative heat. *Int. J. Appl. Comput. Math.* **2017**, *3*, 561–578. [[CrossRef](#)]
11. Sharada, K.; Shankar, B. MHD mixed convection flow of a Casson fluid over an exponentially stretching surface with the effects of Soret, Dufour, thermal radiation and chemical reaction. *World J. Mech.* **2015**, *5*, 165. [[CrossRef](#)]
12. Ullah, I.; Bhattacharyya, K.; Shafie, S.; Khan, I. Unsteady MHD mixed convection slip flow of Casson fluid over nonlinearly stretching sheet embedded in a porous medium with chemical reaction, thermal radiation, heat generation/absorption and convective boundary conditions. *PLoS ONE* **2016**, *11*, e0165348. [[CrossRef](#)] [[PubMed](#)]
13. Ullah, I.; Khan, I.; Shafie, S. Hydromagnetic Falkner-Skan flow of Casson fluid past a moving wedge with heat transfer. *Alex. Eng. J.* **2016**, *55*, 2139–2148. [[CrossRef](#)]
14. Pushpalatha, K.; Sugunamma, V.; Reddy, J.R.; Sandeep, N. Heat and mass transfer in unsteady MHD Casson fluid flow with convective boundary conditions. *Int. J. Adv. Sci. Technol.* **2016**, *91*, 19–38. [[CrossRef](#)]
15. Pushpalatha, K.; Reddy, J.R.; Sugunamma, V.; Sandeep, N. Numerical study of chemically reacting unsteady Casson fluid flow past a stretching surface with cross diffusion and thermal radiation. *Open Eng.* **2017**, *7*, 69–76. [[CrossRef](#)]
16. Uddin, M.J.; Khan, W.; Ismail, A.M. Free convection boundary layer flow from a heated upward facing horizontal flat plate embedded in a porous medium filled by a nanofluid with convective boundary condition. *Transp. Porous Media* **2012**, *92*, 867–881. [[CrossRef](#)]
17. Rahman, M.; Al-Lawatia, M.; Eltayeb, I.; Al-Salti, N. Hydromagnetic slip flow of water based nanofluids past a wedge with convective surface in the presence of heat generation (or) absorption. *Int. J. Therm. Sci.* **2012**, *57*, 172–182. [[CrossRef](#)]
18. Das, K. Slip flow and convective heat transfer of nanofluids over a permeable stretching surface. *Comput. Fluids* **2012**, *64*, 34–42. [[CrossRef](#)]
19. Ibrahim, W.; Shankar, B. MHD boundary layer flow and heat transfer of a nanofluid past a permeable stretching sheet with velocity, thermal and solutal slip boundary conditions. *Comput. Fluids* **2013**, *75*, 1–10. [[CrossRef](#)]
20. Abbas, Z.; Wang, Y.; Hayat, T.; Oberlack, M. Slip effects and heat transfer analysis in a viscous fluid over an oscillatory stretching surface. *Int. J. Numer. Methods Fluids* **2009**, *59*, 443–458. [[CrossRef](#)]
21. Makinde, O.D.; Mabood, F.; Ibrahim, M.S. Chemically reacting on MHD boundary-layer flow of nanofluids over a non-linear stretching sheet with heat source/sink and thermal radiation. *Therm. Sci.* **2018**, *22*, 495–506. [[CrossRef](#)]
22. Ibrahim, S.; Kumar, P.; Lorenzini, G.; Lorenzini, E.; Mabood, F. Numerical study of the onset of chemical reaction and heat source on dissipative MHD stagnation point flow of Casson nanofluid over a nonlinear stretching sheet with velocity slip and convective boundary conditions. *J. Eng. Thermophys.* **2017**, *26*, 256–271. [[CrossRef](#)]
23. Prasannakumara, B.; Krishnamurthy, M.; Gireesha, B.; Gorla, R.S. Effect of multiple slips and thermal radiation on MHD flow of Jeffery nanofluid with heat transfer. *J. Nanofluids* **2016**, *5*, 82–93. [[CrossRef](#)]
24. Imtiaz, M.; Hayat, T.; Alsaedi, A.; Hobiny, A. Homogeneous-heterogeneous reactions in MHD flow due to an unsteady curved stretching surface. *J. Mol. Liq.* **2016**, *221*, 245–253. [[CrossRef](#)]
25. Mabood, F.; Shateyi, S. Multiple Slip Effects on MHD Unsteady Flow Heat and Mass Transfer Impinging on Permeable Stretching Sheet with Radiation. *Model. Simul. Eng.* **2019**, *2019*, 1–11. [[CrossRef](#)]

26. Malarselvi, A.; Bhuvaneswari, M.; Sivasankaran, S.; Ganga, B.; Hakeem, A.A. Effect of Slip and Convective Heating on Unsteady MHD Chemically Reacting Flow Over a Porous Surface with Suction. In *Applied Mathematics and Scientific Computing*; Springer: Cham, Switzerland, 2019; pp. 357–365.
27. Singh, K.; Kumar, M. Effect of viscous dissipation on double stratified MHD free convection in micropolar fluid flow in porous media with chemical reaction, heat generation and ohmic heating. *Chem. Process Eng. Res.* **2015**, *31*, 75–80.
28. Rana, P.; Bhargava, R.; Bég, O.A. Finite element simulation of unsteady magneto-hydrodynamic transport phenomena on a stretching sheet in a rotating nanofluid. *Proc. Inst. Mech. Eng. Part N J. Nanoeng. Nanosyst.* **2013**, *227*, 77–99. [[CrossRef](#)]
29. Reddy, J.N. *An Introduction to the Finite Element Method*; McGraw-Hill Education: New York, NY, USA, 1993.
30. Swapna, G.; Kumar, L.; Rana, P.; Singh, B. Finite element modeling of a double-diffusive mixed convection flow of a chemically-reacting magneto-micropolar fluid with convective boundary condition. *J. Taiwan Inst. Chem. Eng.* **2015**, *47*, 18–27. [[CrossRef](#)]
31. Gupta, D.; Kumar, L.; Beg, O.A.; Singh, B. Finite-element analysis of transient heat and mass transfer in microstructural boundary layer flow from a porous stretching sheet. *Comput. Therm. Sci. Int. J.* **2014**, *6*. [[CrossRef](#)]
32. Crane, L.J. Flow past a stretching plate. *Z. Für Angew. Math. Und Phys. ZAMP* **1970**, *21*, 645–647. [[CrossRef](#)]
33. Gireesha, B.; Ramesh, G.; Bagewadi, C. Heat transfer in MHD flow of a dusty fluid over a stretching sheet with viscous dissipation. *J. Appl. Sci. Res.* **2012**, *3*, 2392–2401.
34. Jalil, M.; Asghar, S.; Yasmeen, S. An exact solution of MHD boundary layer flow of dusty fluid over a stretching surface. *Math. Probl. Eng.* **2017**, 2017. [[CrossRef](#)]
35. Ishak, A.; Nazar, R.; Pop, I. Boundary layer flow and heat transfer over an unsteady stretching vertical surface. *Meccanica* **2009**, *44*, 369–375. [[CrossRef](#)]
36. Uddin, M.; Rana, P.; Bég, O.A.; Ismail, A.M. Finite element simulation of magnetohydrodynamic convective nanofluid slip flow in porous media with nonlinear radiation. *Alex. Eng. J.* **2016**, *55*, 1305–1319. [[CrossRef](#)]
37. Chamkha, A.; Aly, A.; Mansour, M. Similarity solution for unsteady heat and mass transfer from a stretching surface embedded in a porous medium with suction/injection and chemical reaction effects. *Chem. Eng. Commun.* **2010**, *197*, 846–858. [[CrossRef](#)]
38. Ali, M.E. Heat transfer characteristics of a continuous stretching surface. *Wärme-Und Stoffübertragung* **1994**, *29*, 227–234. [[CrossRef](#)]
39. Pal, D. Combined effects of non-uniform heat source/sink and thermal radiation on heat transfer over an unsteady stretching permeable surface. *Commun. Nonlinear Sci. Numer. Simul.* **2011**, *16*, 1890–1904. [[CrossRef](#)]
40. Haile, E.; Shankar, B. Heat and mass transfer in the boundary layer of unsteady viscous nanofluid along a vertical stretching sheet. *J. Comput. Eng.* **2014**, 2014. [[CrossRef](#)]

